




Fermi surface of the magnetic kagome compound GdV_6Sn_6 investigated using de Haas–van Alphen oscillations

C. Dhital ^{1,*}, G. Pokharel ², B. Wilson,¹ I. Kendrick,¹ M. M. Asmar ¹, D. Graf,³ J. Guerrero-Sanchez,⁴ R. Gonzalez-Hernandez,⁵ and S. D. Wilson²

¹*Department of Physics, Kennesaw State University, Marietta, Georgia 30060, USA*

²*Materials Department and California NanoSystems Institute, University of California Santa Barbara, Santa Barbara, California 93106, USA*

³*National High Magnetic Field Laboratory, Tallahassee, Florida 32310, USA*

⁴*Centro de Nanociencias y Nanotecnología, Universidad Nacional Autónoma de México, Ensenada, BC 22860, México*

⁵*Departamento de Física y Geociencias, Universidad del Norte, Barranquilla 080020, Colombia*



(Received 29 June 2023; revised 24 February 2024; accepted 6 June 2024; published 24 June 2024)

The shape of the Fermi surface, and the cyclotron effective mass of the kagome magnet GdV_6Sn_6 charge carriers are investigated using de Haas–van Alphen (dHvA) oscillation measurements and electronic band structure calculations. The temperature- and angle-dependent torque magnetometry measurements revealed at least nine different frequencies ranging from ~ 10 T up to ~ 9000 T. These frequencies correspond to extremal areas of the Fermi surface ranging from $\sim 0.2\%$ up to 50% of the first Brillouin zone, qualitatively consistent with the electronic band structure calculations. The angle-dependent dHvA oscillation frequencies indicate that the smaller pockets of the Fermi surface have an almost three-dimensional character whereas the bigger pockets of the Fermi surface are mostly two dimensional. We also find evidence of the presence of light [$0.28(1)m_0$] as well as heavy [$2.37(18)m_0$] charge carriers through the analysis of the temperature dependence of dominant frequencies. The comparison of the observed frequencies with the electronic band structure calculations indicates that the heavy masses correspond to saddle-point-like features of electronic band structure at the M point. The observation of the multiple low frequencies and the calculated contributions from various bands to such low frequencies prevent the estimation of the topological nature of bands containing lighter fermions. In conclusion, our work reveals the features of a Fermi surface containing enhanced mass fermions originating from saddle points in the electronic band structure at the M point, which is inherent to kagome lattices.

DOI: [10.1103/PhysRevB.109.235145](https://doi.org/10.1103/PhysRevB.109.235145)

I. INTRODUCTION

The kagome lattice, a two-dimensional network of corner-sharing triangles of metal ions, is known to be a source of a variety of novel correlated electronic states [1–5]. The flat bands representing the correlated electronic states, the Dirac fermions featuring topological electronic states, and the saddle point derived Van Hove singularities causing novel electronic instabilities are typical features of kagome lattice materials [4]. Chiral charge density waves [6], Chern topological magnetism [7], and topological superconductivity [2,3,5] are some of the new electronic phases that have been observed in materials with kagome lattice structures.

The list of kagome metals includes chemically diverse compounds such as Mn_3Sn [8], Fe_3Sn_2 [9,10], $\text{Co}_3\text{Sn}_2\text{S}_2$ [11–13], CoSn [14], FeSn [14], AV_3Sb_5 ($A = \text{Rb}, \text{Cs}, \text{K}$) [14], RM_6X_6 ($R = \text{Li/Mg/Yb/Sm/Gd/Ho/Tb/Y}$, $M = \text{Fe/Cr/Co/Ni/V}$, and $X = \text{Ge/Sn/Si}$) [7,15–22]. Such chemical diversity combined with layered crystal structures allows for fine tuning of intra- and inter-kagome-layer interactions to realize novel electronic and magnetic phases. The family that draws particular attention is RM_6X_6 . The RM_6X_6 struc-

ture contains two-dimensional parallel kagome layers of M ions coordinated by X ions and separated by the triangular planes of R ions. One advantage of such structure is that the inter-kagome-layer distances can be tuned by changing the size of R ions whereas the magnetic interactions can be varied by choosing the magnetic and nonmagnetic R and M ions. Furthermore, the intrinsic physics associated with the kagome layer can be separated from the spacer layers by a suitable choice of elements. The work presented in this paper is focused on the study of GdV_6Sn_6 , in which the nonmagnetic V_3Sn_2 kagome layers are separated by magnetic GdSn triangular planes and Sn atoms as shown in Fig. 1.

Previous studies on GdV_6Sn_6 indicate a noncollinear magnetic ground state ($T_N \sim 5$ K) arising from the f orbitals of Gd ions along with a high-mobility multiband electrical transport originating from the correlated electrons in the kagome layers [18–23]. The electronic band structure calculations as well as photoemission experiments indicate the presence of chemically tunable Dirac surface states (DSSs) [21,23], flat bands, and Van Hove singularities featuring the intrinsic physics of the kagome lattice [21–23]. Despite such studies, a detailed experimental investigation of the shape of the bulk Fermi surface, cyclotron effective mass of carriers, and observables featuring the topologically nontrivial bands and the saddle points causing Van Hove singularity are still missing.

*Contact author: cdhital@kennesaw.edu

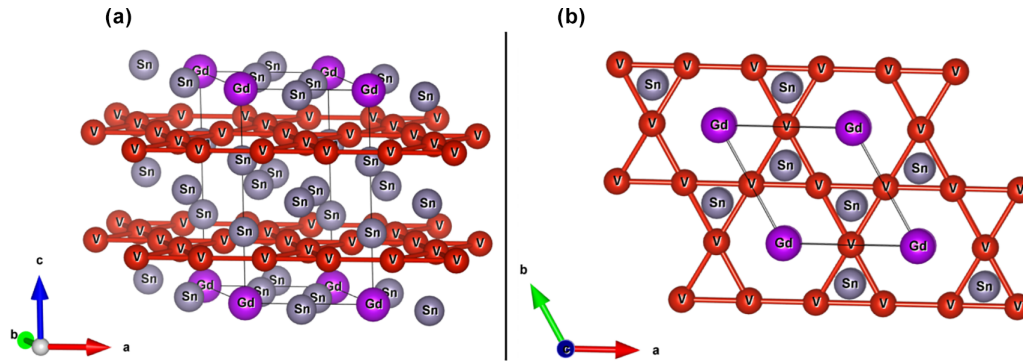


FIG. 1. Crystal structure of GdV_6Sn_6 . (a) Crystal structure showing different layers of Gd, Sn, and V atoms. (b) Crystal structure viewed along the c axis showing the kagome network of V atoms. The colored spheres indicate different atoms.

Such experimental investigations can be carried out using de Haas–van Alphen (dHvA) oscillations or Shubnikov–de Haas (SdH) oscillations. One previous study [19] of GdV_6Sn_6 uses SdH oscillations measurement of electrical resistivity. That previous study reports observations of two small frequencies, 150 and 200 T, accounting for small Fermi pockets occupying about 2.5% of the area of the first Brillouin zone. However, no other features revealing the relativistic nature of Dirac fermions and the saddle points in the electronic band structures were reported. In this work, we have used high-field torque magnetometry measurements to study the dHvA oscillations. One advantage of the dHvA oscillations measurement is that the magnetization oscillation directly originates from the oscillations of the free electrons' energy and does not rely on scattering probabilities. By using a single-crystalline sample of residual resistivity ratio (RRR ~ 12), we are able to observe dHvA oscillations on top of a magnetic background of $\sim 7 \mu_B$. We have extracted several oscillation frequencies ranging from 10–9000 T indicating the presence of small and big pockets of the Fermi surfaces, consistent with the multiband nature of electrical transport and the calculated electronic band structure. The angular dependence of the oscillation frequencies indicates the presence of mostly three-dimensional (3D) small pockets and quasi-two-dimensional (2D) type big pockets of the Fermi surfaces. The temperature dependence of the oscillation amplitudes indicates the presence of both light electrons ($0.28 m_0$) and heavier electrons ($2.37 m_0$). Some bands cross the Fermi level more than one time giving different effective masses. The observation of multiple low frequencies (< 500 T), the calculated contributions from various bands, and crossing of the Fermi level by the same band more than one time prevent the estimation of the Berry curvature associated to topologically nontrivial bands. However, we are able to clearly observe and resolve other features associated with enhanced mass fermions that characterize kagome materials such as the saddle points in the proximity of the M point in the Brillouin zone.

II. EXPERIMENTAL DETAILS

Single crystals of GdV_6Sn_6 were synthesized via a flux-based technique. Gd (pieces, 99.9%), V (pieces, 99.7%), and Sn (shot, 99.99%) were loaded inside an alumina crucible with the molar ratio of 1:6:20 and then heated at 1125°C for

12 h. Then the mixture was cooled at a rate of $2^\circ\text{C}/\text{h}$. The single crystals were separated from the flux via centrifuging at 780°C . Crystals grown via this method were generally a few millimeters long and < 1 mm in thickness. The separated single crystals were subsequently cleaned with dilute HCl to remove any flux contamination. Crystals were then transferred into a small jar of mercury to remove any additional tin contamination. Single-crystal x-ray diffraction measurements were carried out on a Kappa APEXII single-crystal diffractometer with a charge coupled device (CCD) detector and a Mo source. The low-field magnetization measurements were carried out using a Quantum Design Magnetic Properties Measurement Systems (MPMS-3). The resistivity was measured using four probe methods employing the electrical transport option (ETO) of the Quantum Design Dynacool Physical Properties Measurement System.

High-field measurements were carried out at the National High Magnetic Field Laboratory (NHMFL), Tallahassee, Florida, with the maximum applied fields of 18 T (superconducting magnet), and 35 T (dc resistive water-cooled magnet). In both experiments the lowest temperature of 0.35 K was achieved using a top-loaded ^3He insert. The magnetic torque was measured using a miniature piezoresistive cantilever. A tiny GdV_6Sn_6 crystal was selected and then fixed to the cantilever arm with vacuum grease. The cantilever was subsequently mounted on the rotating platform of a special probe designed at NHMFL. The probe was then slowly cooled down to the base temperature of 0.35 K. Two resistive elements on the cantilever were incorporated with two other room-temperature resistors to form a Wheatstone bridge, which was balanced at base temperature before taking field-dependent data. The angle-dependent torque data were obtained by rotating the sample *in situ* with the applied field. Magnetic fields were swept at each fixed temperature at a rate of 2.7 T/min (up) and 4.2 T/min (down).

III. COMPUTATIONAL METHODS

The electronic band structure calculations were done using the Vienna *Ab Initio* Simulation Package (VASP) [24–26]. The electron–electron nonclassical exchange–correlation interactions were modeled using the generalized gradient approximation under the Perdew–Burke–Ernzerhof (PBE) parametrization [27]. Projected augmented wave potentials

[25,28] were used with an optimized cutoff energy of 520 eV. Energy and force criteria were applied to reach structural relaxation, where the energy and norms of all forces must be less than 10^{-6} eV and 0.01 eV/Å, respectively. A discrete equally spaced mesh [29] of $10 \times 10 \times 6$ k points was used to evaluate the electronic states during the ionic relaxation process. For the electronic band structure analysis, the convergence criterion was taken as the condition where the total energy change between two successive iterations in the self-consistent loop became smaller than 10^{-8} eV. For the converged calculations, a k -point mesh of $15 \times 15 \times 12$ was used. Since we are treating atoms with large atomic mass—where relativistic effects take importance, spin-orbit coupling interactions are mandatory—we also included it in the relaxation and electronic properties of the GdV_6Sn_6 structure. Also, f orbitals of the Gd atom with highly localized electrons must be accounted for. To do so, we included the Hubbard interaction in the simplified approach proposed by Dudarev *et al.* [30], with an on-site Coulomb parameter $U = 6$ eV for the Gd atom. To calculate the Fermi energy in a dense k mesh ($121 \times 121 \times 123$), we have used the Hamiltonian based on the Wannier functions obtained using the WANNIER90 code [31]. We modeled the GdV_6Sn_6 material considering the hexagonal $P6/mmm$ space group in its ferromagnetic structure. The dHvA frequencies and their angular dependencies were calculated via the SKEAF code [32].

IV. RESULTS

The room-temperature x-ray diffraction pattern from the flat surface of a single crystal of GdV_6Sn_6 is presented in Fig. 2(a). The peaks can be indexed with hexagonal structure with space group $P6/mmm$. The diffraction pattern contains only peaks corresponding to Miller indices $(00l, l = 1, 2, 3 \dots)$ indicating that the flat surface is perpendicular to the crystalline c axis. The magnetic susceptibility of a single crystal under a field of 1 kOe applied along the c axis is presented in Fig. 2(b). The susceptibility follows a typical Curie-Weiss behavior at higher temperatures; however, it enters a long-range magnetic phase around $T_N \approx 5$ K. The inset in Fig. 2(b) displays the fitting to Curie-Weiss behavior $\frac{1}{\chi} = \chi_0 + \frac{C}{T - \theta_C}$ ($T > 20$ K) with the Curie constant (C), a Curie-Weiss temperature (θ_C), and a small background term (χ_0). The fitting yields $C = 7.307(2)$ emu mol $^{-1}$ Oe $^{-1}$ K, $\theta_C = 7.96(2)$ K, and $\chi_0 = 0.002(1)$ emu mol $^{-1}$ Oe $^{-1}$ K. This gives effective moment $\mu_{\text{eff}} = 7.7(2) \mu_B/\text{f.u.}$ consistent with the expected full moment from the Gd^{3+} ion ($7.94 \mu_B$). The positive Curie-Weiss temperature indicates the dominant ferromagnetic interactions along the c axis. Figure 2(c) presents the zero-field electrical resistivity as a function of temperature for a GdV_6Sn_6 single crystal with current within the ab plane. The resistivity exhibits typical metallic behavior with a small downturn at the magnetic transition (5 K), indicating the interaction between $3d$ itinerant electrons in the kagome layer and the Gd spins in the spacer layer. The residual resistivity ratio ($\text{RRR} \approx 12$) allows the measurement of the dHvA oscillations in the presence of a uniform magnetic background. A more detailed investigation of the structural, electrical, and magnetic properties of GdV_6Sn_6 indicating the onset of

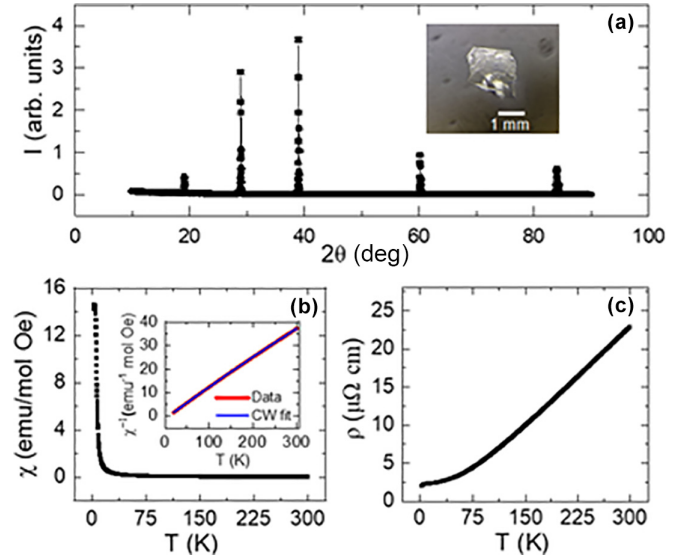


FIG. 2. Single-crystal characterization of GdV_6Sn_6 . (a) X-ray diffraction pattern observed from the flat surface of a single crystal (shown in inset) of GdV_6Sn_6 . The presence of only sharp $(00l)$ type reflections indicates a high-quality single-domain crystal with the c axis perpendicular to the flat surface. (b) Magnetic susceptibility χ as a function of temperature measured at 1 kOe field applied parallel to the c axis. The inset shows Curie-Weiss law fitting for $T > 20$ K. (c) Zero-field electrical resistivity ρ with current within the ab plane.

long-range magnetic order with a large, saturated moment ($\sim 7 \mu_B$) is reported in a previous electrical transport study [22]. Our computational findings ($7.07 \mu_B$ per Gd ion and multiband nature) are consistent with the results of that previous electrical transport study [22].

The results of typical magnetic torque measurements are presented in Fig. 3. Figure 3(a) presents the magnetic torque (τ) as a function of magnetic field (H) at $\theta = -10^\circ$ and $+7^\circ$ measured using the 18 T superconducting magnet and the 35 T resistive magnets, respectively. Here, θ is the angle between the magnetic field and the c axis of the crystal as shown in the inset of Fig. 3(a) and the sign of θ represents the sense of rotation of the magnetic field with respect to the c axis of the crystal. Figure 3(b) displays the third-order polynomial background subtracted signal ($\Delta\tau$) as function of inverse magnetic field ($1/H$) at given angles indicating quantum oscillations that are periodic in $1/H$. Figure 3(c) displays the Fourier transformation of background subtracted signals at $\theta = 0^\circ$, $T = 0.35$ K for different fast Fourier transformation (FFT) ranges.

The x axis of Fig. 3(c) is displayed in a logarithmic scale to highlight the low frequencies. At $\theta = 0^\circ$, we observe nine dominant frequencies, $F_1 = (13 \pm 7)$ T, $F_2 = (32 \pm 10)$ T, $F_3 = (95 \pm 10)$ T, $F_4 = (176 \pm 6)$ T, $F_5 = (200 \pm 10)$ T, $F_6 = (850 \pm 20)$ T, $F_7 = (1470 \pm 30)$ T, $F_8 = (8440 \pm 50)$ T, and $F_9 = (8850 \pm 60)$ T, that are consistent with the electronic band structure calculations. These frequencies correspond to four different bands (α , β , γ , and δ) present at the Fermi level. We also observe frequencies having weak amplitudes around 55, 290, 390, 1040, and 1370 T. However, due to the presence of nearby frequencies with strong amplitudes, we are

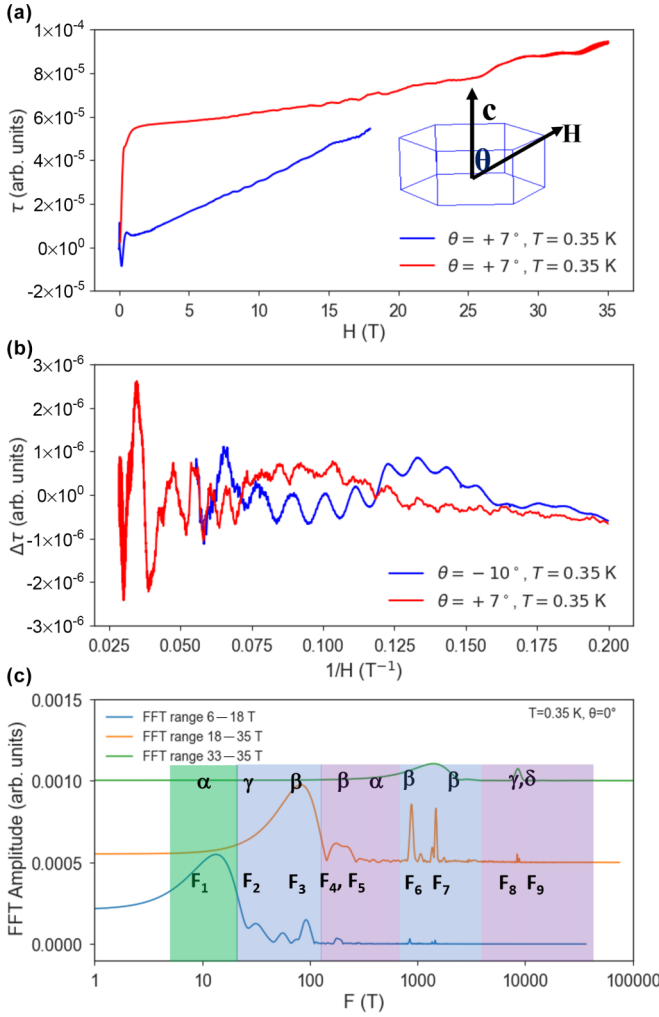


FIG. 3. Magnetic torque measurements: (a) The magnetic torque (τ) as a function of magnetic field (H) taken using the 18 T (blue) and the 35 T (red) magnet at given angles. The inset figure shows the schematic of the magnetic field direction relative to crystal axes. (b) The polynomial background subtracted signal ($\Delta\tau$) as a function of the inverse magnetic field ($1/H$). (c) The fast Fourier transform (FFT) spectra (amplitude vs frequency) at $\theta = 0^\circ$, $T = 0.35$ K, for FFT ranges of 6–18 T, 18–35 T, and 33–35 T. The x axis is plotted in logarithmic scale to highlight features at low frequencies. The frequencies $F_1 - F_9$ in (c) represent dominant frequencies. The symbols (α , β , γ , δ) represent possible bands contributing to those frequencies as indicated by shaded regions.

unable to track down the temperature and angle dependence of all frequencies. We therefore focus on the analysis of six frequencies ($F_1, F_3, F_6, F_7, F_8, F_9$) mentioned above and displayed in Fig. 3(c). After identifying the frequencies at $\theta = 0^\circ$, the angle-dependent torque measurements are performed to understand the shape of the Fermi surface. Figure 4 displays the results of angle-dependent measurements at $T = 0.35$ K. For the analysis of low frequencies ($F < 500$ T), the FFT range of 6–18 T is used whereas for frequencies $F > 500$ T, the FFT range of 18–35 T is used. As is clear from Figs. 3(c) and 4, we observe many frequencies below 500 T, making it difficult to follow the angle dependence of every frequency.

The low frequencies (F_1, F_2, F_3, F_4, F_5) survive at all angles between 0° and -90° with some angle dependence. The frequencies F_6 and F_7 appear only between $\theta = 0^\circ$ and $\theta = -10^\circ$ and disappear quickly. The high frequencies F_8, F_9 disappear above $\theta = -50^\circ$. This indicates that the Fermi surface contains small pockets of mostly 3D shape and bigger pockets of 2D shapes. It is important to note that out of these frequencies observed in this work, only two nearby frequencies of 150 and 200 T were reported in the previous work [19] using SdH oscillations.

The observed frequencies are compared to those expected from electronic band structure calculations. The results are summarized in Fig. 5. The electronic structure calculated frequencies from the different bands are plotted as colored symbols (orange upward triangle, gray downward triangle, red diamond, green left triangle) whereas the observed frequencies are plotted as a black circle. The calculated frequencies for the four bands (α , β , γ , and δ) closely match those observed experimentally. The next step is to study the temperature dependence of these frequencies. By suitably choosing the FFT range and the angle, the temperature dependences of F_1, F_3, F_6, F_7, F_8 , and F_9 are studied in this work. The temperature dependences of F_1, F_3, F_8 and F_9 are studied using data taken at $\theta = -10^\circ$ whereas the temperature dependences of F_6 and F_7 are studied using data taken at $\theta = 0^\circ$. We used an FFT range of 6–8 T to study the temperature variations of F_1, F_3 , and F_5 whereas we used a FFT range of 14–18 T to study the temperature variations of F_6 and F_7 . The variations of normalized FFT amplitudes with temperature for F_1, F_3, F_6, F_7, F_8 , and F_9 are presented in Fig. 6. These variations can be described by the damping part of the Lifshitz-Kosevich (LK) formula [33,34] (solid lines in Fig. 6). Fitting with the LK formula gives six different effective masses $m_1^* = 0.28(1)m_0$, $m_3^* = 0.36(1)m_0$, $m_6^* = 1.20(6)m_0$, $m_7^* = 0.79(5)m_0$, $m_8^* = 2.25(15)m_0$, and $m_9^* = 2.37(18)m_0$. The details of the LK fitting are presented in Appendix B.

Along with the determination of the effective mass (m^*) using the LK formula, the different areas associated with different sections of the Fermi surface are estimated using the Onsager relation [34]. We then calculate the Dingle temperature T_D (an additional temperature factor that accounts for the damping of oscillations amplitude with inverse field). The estimation of the Dingle temperature is presented in Appendix B. After calculating the extremal area (S_f), Fermi wave vector (k_f), effective mass (m^*), and Dingle temperature (T_D), we estimate the Fermi velocity (v_f), quantum scattering time (τ_s), mean free path (l_D), and the quantum mobility (μ). We define μ as quantum mobility to distinguish it from the classical mobility arising from the Drude model that can be present without a magnetic field. In this case, mobility is related to the cyclotron motion of carriers. These quantities are presented in Table I.

After establishing the presence of multiple pockets of the Fermi surface, the next conventional step in such analysis would be the estimation of the Berry phase (ϕ_B) by analyzing the oscillatory part of the LK formula [34,35]: $\sin[2\pi(\frac{F}{H} + \frac{q_B}{2\pi} - \frac{1}{2} + \delta_p)]$ where the factor δ_p depends upon the dimensionality of the Fermi pocket and takes the value $+\frac{1}{8}$ for the minimal and $-\frac{1}{8}$ for maximal cross sections of a

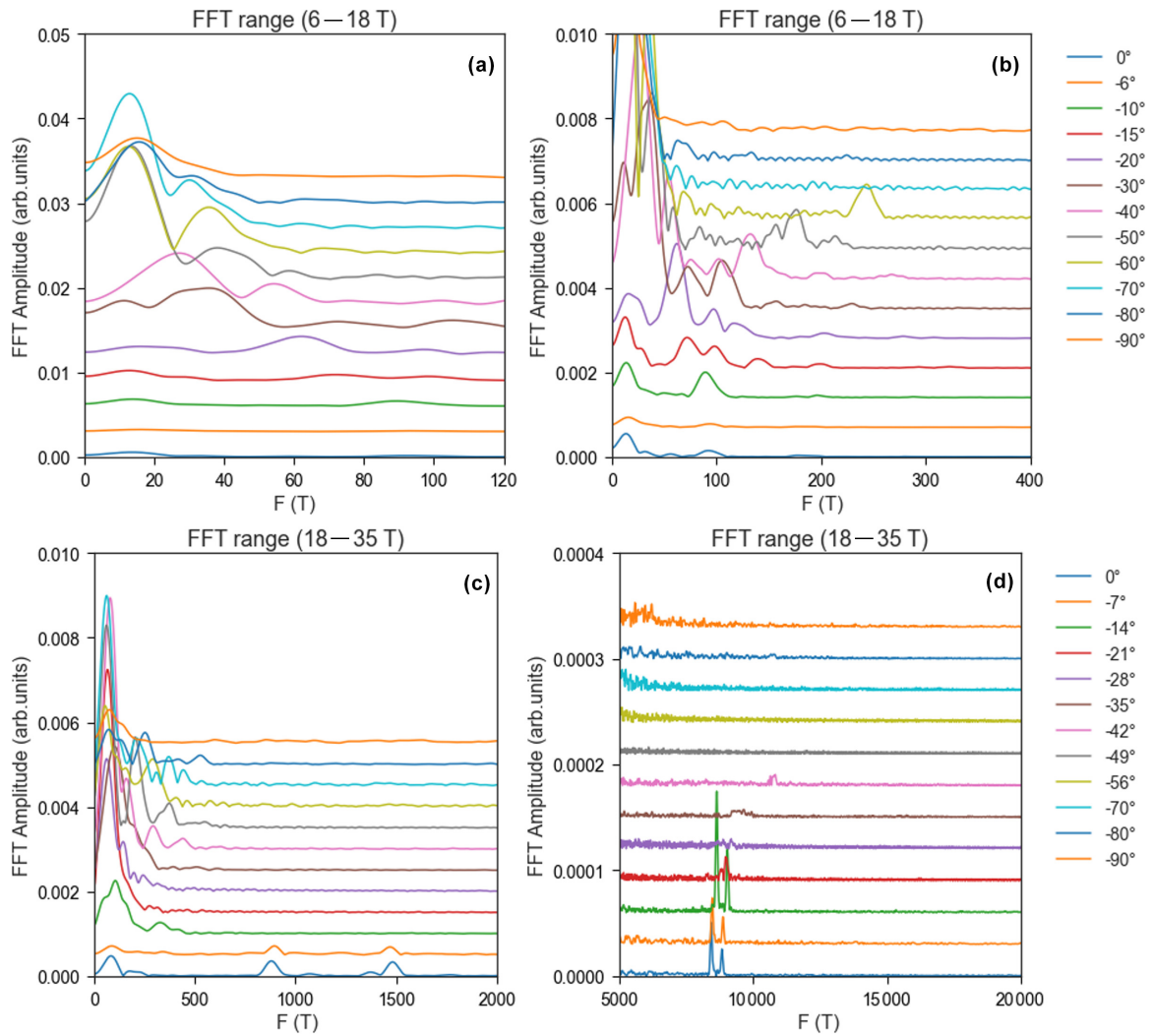


FIG. 4. Angle dependence of dHvA oscillation frequencies at $T = 0.35$ K. (a), (b) Frequencies obtained with FFT range of 6–18 T. (c), (d) Frequencies obtained with FFT range of 18–35 T.

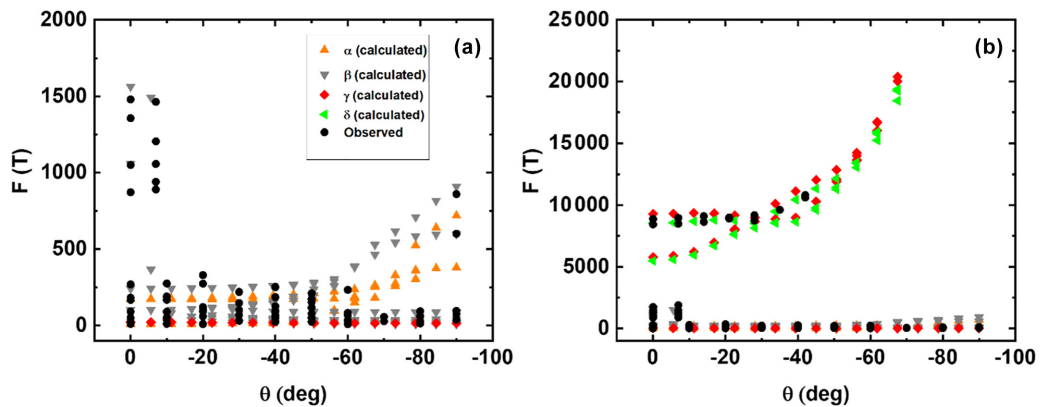


FIG. 5. (a) Angle dependence of electronic band structure calculated frequencies (α , β , γ , δ) and observed frequencies (\bullet). The observed frequencies are taken at $T = 0.35$ K. Different colors of calculated frequencies represent different bands. (a) Observed and calculated frequencies below 2000 T. The shaded region in (a) contains at least two frequencies (F_6 and F_7) related to two orbits containing the β band. The other frequencies in (a) contain contributions from at least three different orbits associated to α , β , and γ bands. (b) All observed and calculated frequencies. The frequencies above 5000 T in (b) correspond to γ and δ bands (F_8 , F_9), respectively.

TABLE I. Results of dHvA oscillations showing observed frequencies (F), extremal orbit area (S_f), Fermi wave vector (k_f), effective mass (m^*), Fermi velocity (v_f), Dingle temperature (T_D), quantum scattering time (τ_s), mean free path (l_D), and quantum mobility (μ). The numbers in parentheses indicate the errors.

F (T)	S_f (\AA^{-2})	k_f (\AA^{-1})	m^*/m_0	v_f ($\times 10^4$ m s $^{-1}$)	T_D (K)	τ_s ($\times 10^{-13}$ s)	l_D (nm)	μ (cm 2 V $^{-1}$ s $^{-1}$)
95 (10)	0.009(1)	0.053(2)	0.36(1)	17(1)	13.1(2)	0.92(1)	16(1)	453(14)
850 (20)	0.081(1)	0.161(1)	1.21(1)	15.3(2)	10.2(3)	1.19(3)	18(1)	173(5)
1470 (30)	0.141(2)	0.211(2)	0.79(5)	31(2)	22(1)	0.55(2)	17(1)	123(9)
8440 (50)	0.802(4)	0.506(1)	2.25(15)	26(2)	4.1(2)	2.9(1)	77(4)	231(19)

three-dimensional Fermi surface. The factor of $\frac{1}{2}$ comes from Maslov correction and applies to the case where the orbits are compressible to circles [36].

It has been suggested in recent works [35,37,38] that the precise estimation of Berry phase requires understanding the details of crystalline and magnetic symmetries of materials. Therefore, a phase of π should not be taken as smoking gun proof of nontrivial topology. In our experimental study, we encountered a notable complication stemming from the presence of numerous closely spaced frequencies, all falling below the 500 T threshold. This intricate frequency landscape presents a significant challenge, rendering the precise estimation of the Berry phase inconclusive. However, unlike the Berry phase that could be blurred by multiple close frequencies, the mass enhancement associated to the saddle points in electronic band structure is clearly observed and reproduced by electronic band structure calculations.

V. DISCUSSION AND CONCLUSIONS

Our dHvA-based analysis of GdV₆Sn₆ revealed several important features revealing this kagome material's Fermi surface properties. We observed nine dominant frequencies $\{F_1 = (13 \pm 7)$ T, $F_2 = (32 \pm 10)$ T, $F_3 = (95 \pm 10)$ T, $F_4 = (176 \pm 6)$ T, $F_5 = (200 \pm 10)$ T, $F_6 = (850 \pm 20)$ T, $F_7 = (1470 \pm 30)$ T, $F_8 = (8440 \pm 50)$ T, and $F_9 =$

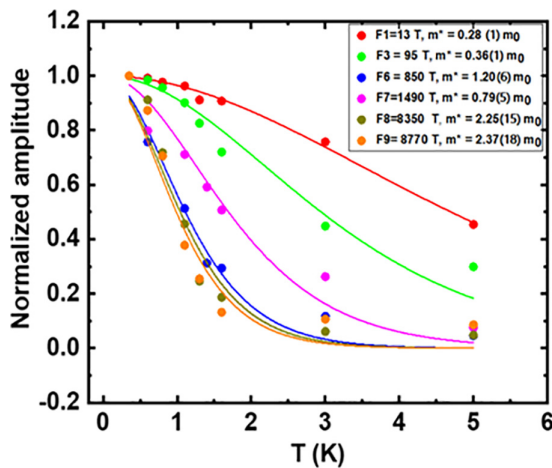


FIG. 6. Temperature dependence of amplitudes of dominant frequencies. Data for F_6 and F_7 were taken from $\theta = 0^\circ$ measurements while the rest of the data were taken from $\theta = -10^\circ$. The solid lines fit to the damping part of the LK formula described in Appendix B.

(8850 ± 60) T], when the magnetic field is applied perpendicular to the kagome plane ($\theta = 0^\circ$). These frequencies are consistent with electronic band structure calculations. In addition, we observed frequencies with weak amplitudes around 55, 290, 390, 1040, and 1370 T. However, due to the presence of nearby strong amplitude frequencies, we are unable to follow the temperature and angle dependence of all frequencies. The lowest frequency, F_1 , corresponds to less than two periods of oscillation in the FFT range of 6–18 T, but it shows a discernible temperature dependence close to the calculated frequencies from the α and γ bands. The comparison of the observed frequencies with the calculated frequencies indicates that the frequencies F_1 and F_4 are most likely related to orbits originating from the α band; F_2 and F_8 are related to orbits originating from the γ band; $F_3, F_5, F_6,$ and F_7 from the β band; and F_9 from the δ band. Furthermore, the angle dependence of dHvA frequencies indicates that the low ($F < 500$ T) frequencies survive when the magnetic field is rotated $\theta = 0^\circ$ to $\theta = 90^\circ$, indicating small Fermi pockets of mostly 3D shape. We also observed large pockets of the Fermi surface. The two frequencies related to such large Fermi pockets disappear at high angles indicating their quasi-2D nature. These facts are also supported by the calculated frequencies from electronic band structure calculation (Figs. 5 and 7) and the projected Fermi surface presented in Fig. 7(b). Notably, α and β bands exhibit holelike characteristics, while the γ and δ bands predominantly demonstrate electronlike behavior. Regarding the Fermi surface shapes, the α and β bands exhibit irregular lobes or pockets along the M - L high-symmetry path whereas the bands γ and δ display barrel-like shapes with prominent and open regions along the same M - L high-symmetry path, as illustrated in Figs. 7(a) and 7(b). It is to be noted that the FFT range for angle dependence presented here is 6–18 T for low frequencies ($F < 500$ T) and 18–35 T for high frequencies ($F > 500$ T). While changing the FFT window, we are also able to observe (not presented here) the second harmonics at some angles especially for high frequencies ($F > 500$ T).

Furthermore, from the temperature dependence of amplitudes of dominant frequencies, we have estimated the cyclotron effective masses [$m_1^* = 0.28(1)m_0$, $m_3^* = 0.36(1)m_0$, $m_6^* = 1.20(6)m_0$, and $m_7^* = 0.79(5)m_0$, $m_8^* = 2.25(15)m_0$, and $m_9^* = 2.37(18)m_0$]. The light masses correspond to α and β bands whereas the heavy masses (m_8 and m_9) correspond to relatively flat bands (γ and δ) near the saddle point around the M point. Notably, these enhanced mass fermions correspond to vanadium d orbitals near the Van Hove singularity (VHS₂) that is clear from the density of states plot presented

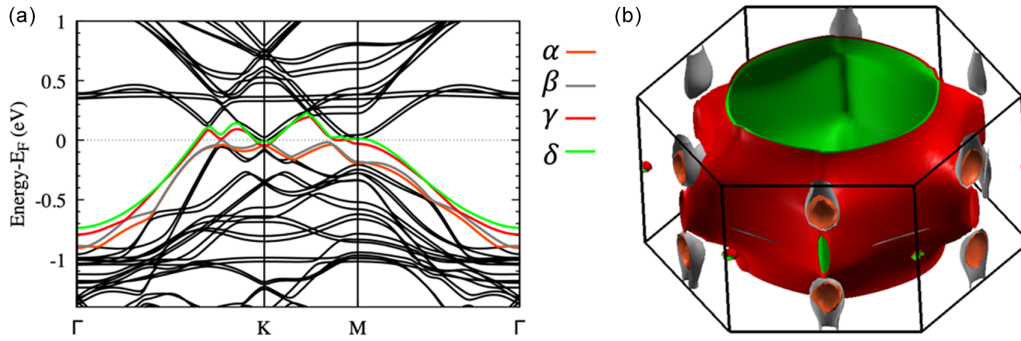


FIG. 7. (a) The electronic band structure of GdV_6Sn_6 in the ferromagnetic state; (b) Fermi surface representation illustrating distinct pockets. The four electronic bands (α , β , γ , and δ) crossing the Fermi level are depicted in distinct colors.

in Fig. 8(b). It is also observed that the calculated quantum mobilities are relatively small compared to other nonmagnetic kagome materials such as CsV_3Sb_5 [39,40]. This is most likely caused by the scattering of electrons from the magnetic background.

Finally, the electronic band structure presented in the current work (Figs. 7 and 8) is in the ferromagnetic state, but it remains largely unchanged in the vicinity of the Fermi level when compared to electronic band structure calculated in the paramagnetic state of TbV_6Sn_6 [41] and GdV_6Sn_6 [22].

This stability is attributed to the f orbitals, crucial for the material's magnetism, being located away from the Fermi level. Moreover, the topological features and saddle points around the Fermi level are dominated by the kagome layer of V atoms.

In summary, our work reveals the Fermi surface of kagome magnet GdV_6Sn_6 with small and big pockets of the Fermi surface consistent with the multiband nature of electrical transport measurements [22]. We found the existence of both lighter ($0.28 m_0$) and heavier ($2.37 m_0$) fermions. While the topological nature of bands contributing to light mass is uncertain, we found clear evidence of enhanced mass fermions originating from the saddle-point-like feature of electronic band structure at the proximity of the M point that led to VHS in the density of states at the Fermi level. The appearance

of such saddle point and corresponding VHS (VHS₂) in the proximity of the Fermi level implies that this system is susceptible to various electronic instabilities.

Note added. Recently, we became aware of similar Fermi surfaces with light and heavy fermions in sister material YV_6Sn_6 [42] reflecting the features of topological nontrivial bands and saddle-point-like features of the electronic band structure of kagome materials.

ACKNOWLEDGMENTS

This work is based upon the work supported by the National Science Foundation under Grant No. DMR- 2213443. We thank J. F. DiTusa for the illuminating discussions. G.P. and S.D.W. acknowledge the support via the UC Santa Barbara NSF Quantum Foundry funded via the Q-AMASE-i program under Award No. DMR-1906325. A portion of this work was performed at the National High Magnetic Field Laboratory, which is supported by the National Science Foundation Cooperative Agreement No. DMR-1644779 and the State of Florida. J.G.-S. acknowledges DGAPA-UNAM Project No. IG101124 for partial financial support. Calculations were performed in the DGCTIC-UNAM Supercomputing Center under Project No. LANCADUNAM-DGTIC-368, LNS-BUAP Project No. 202201042N, and THUBAT KAAL

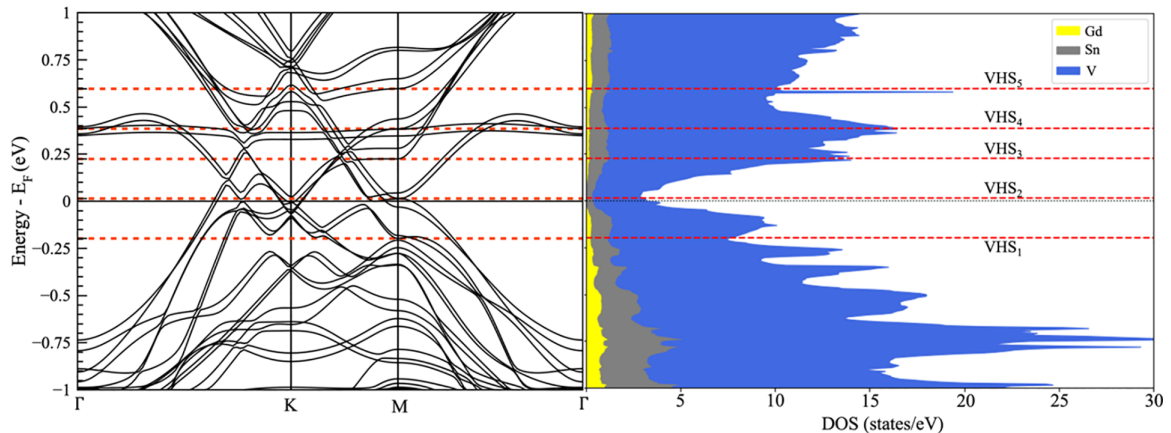


FIG. 8. Band structure of ferromagnetic GdV_6Sn_6 including SOC and projected density of states for the Gd f orbitals (yellow), Sn p orbitals (gray), and V d orbitals (blue). Fermi level is set to zero energy. Dashed lines indicate the energy appearance of the Van Hove singularities (VHS).

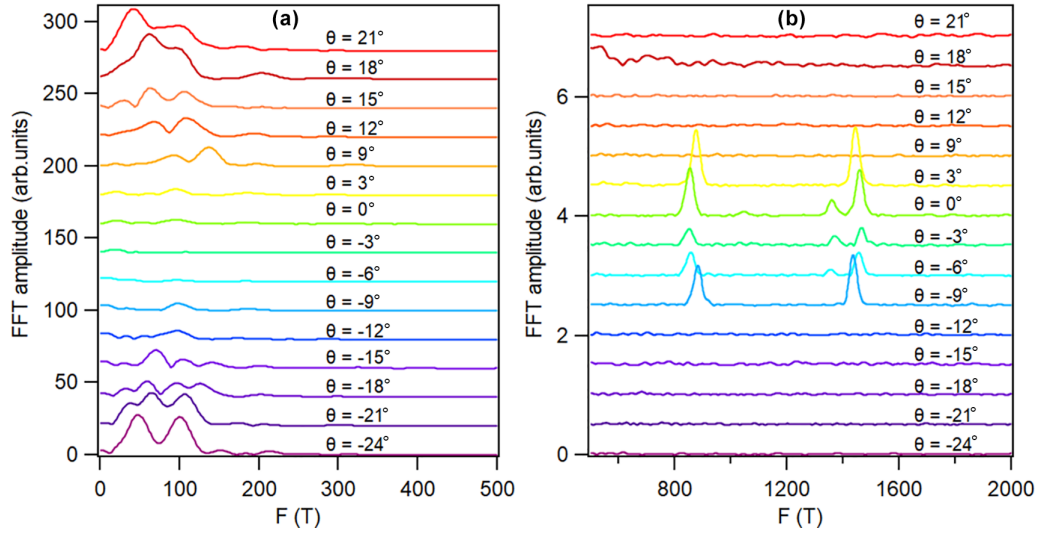


FIG. 9. Small steps angle dependence around $\theta = 0^\circ$ at $T = 0.35$ K. (a) Angle dependence of FFT amplitudes for frequency range 0–500 T. (b) angle dependence of FFT amplitudes for frequency range 500–2000 T.

IPICYT Supercomputing Center Project No. TKII-JGSA001. J.G.-S. also acknowledges A. Rodriguez-Guerrero and E. Murillo for useful discussions and technical assistance. M.M.A. is grateful for the support of the National Science Foundation through Grant No. DMR-2213429.

APPENDIX A: ANGLE DEPENDENCE AROUND $\theta = 0^\circ$

The angle dependencies of FFT frequencies around $\theta = 0^\circ$ are presented in Figs. 9(a) and 9(b). The data were collected using 18 T superconducting magnets at intervals of $\theta = 3^\circ$ – 6° .

APPENDIX B: LIFSHITZ- KOSEVICH (LK) FORMULA, DINGLE TEMPERATURE (T_D), ONSAGER RELATION, FERMI VELOCITY (v_f), SCATTERING RATE (τ_s), MEAN FREE PATH (l_D), AND QUANTUM MOBILITY (μ)

The oscillatory part of the torque is given by [34,43,44]

$$\Delta\tau \propto H^\lambda \frac{A\left(\frac{m^*}{m_0}\right)\frac{T}{\langle H \rangle}}{\sinh\left[A\left(\frac{m^*}{m_0}\right)\frac{T}{\langle H \rangle}\right]} \exp\left\{-A\left(\frac{m^*}{m_0}\right)\frac{T_D}{\langle H \rangle}\right\} \times \cos\left(\pi g \frac{m^*}{2m_0}\right) \sin\left[2\pi\left(\frac{F}{\langle H \rangle} + \psi\right)\right],$$

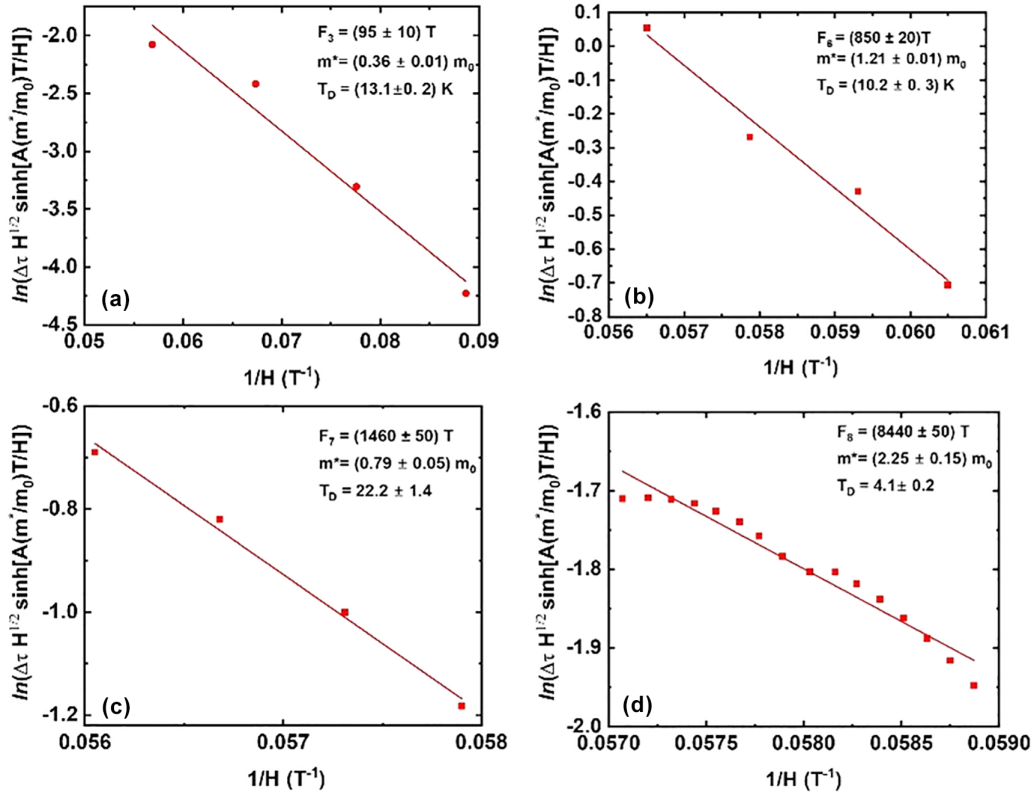
where $\frac{A\left(\frac{m^*}{m_0}\right)\frac{T}{\langle H \rangle}}{\sinh\left[A\left(\frac{m^*}{m_0}\right)\frac{T}{\langle H \rangle}\right]}$ is the thermal damping factor, $\exp\left\{-A\left(\frac{m^*}{m_0}\right)\frac{T_D}{\langle H \rangle}\right\}$ is the Dingle damping factor, T_D is the Dingle temperature, $\cos\left(\pi g \frac{m^*}{2m_0}\right)$ is the spin reduction factor, g is the Lande “ g ” factor, m^* is the effective mass of electrons (holes), m_0 is the mass of free electrons, and the exponent $\lambda \sim 0$ for the 2D Fermi surface, and $\lambda \sim \frac{1}{2}$ for the 3D Fermi surface [34]. The constant A is given by $A = \frac{2\pi^2 k_B m_0}{e\hbar} = 14.69$ T/K. Here $\langle H \rangle$ is the harmonic mean of the minimum and maximum field used in FFT $\left[\frac{1}{\langle H \rangle} = \frac{\left(\frac{1}{H_{\min}} + \frac{1}{H_{\max}}\right)}{2}\right]$. The phase factor ψ is given by $\psi = \left(\varphi - \frac{1}{2}\right)$. The factor φ is given by $\varphi = \frac{\vartheta_B}{2\pi} + \delta_p$. Here

ϑ_B is the Berry phase and δ_p is 0 for 2D and $\pm\frac{1}{8}$ for 3D Fermi surfaces with minimal and maximal cross sections, respectively [44]. The effective mass (m^*) is calculated by fitting the normalized amplitude of oscillations to the thermal damping factor term $\frac{A\left(\frac{m^*}{m_0}\right)\frac{T}{\langle H \rangle}}{\sinh\left[A\left(\frac{m^*}{m_0}\right)\frac{T}{\langle H \rangle}\right]}$. The Dingle temperature T_D is obtained by fitting the Dingle damping factor term $\left[\exp\left\{-A\left(\frac{m^*}{m_0}\right)\frac{T_D}{\langle H \rangle}\right\}\right]$. In practice this is done by finding the slope of $\ln[\Delta\tau H^{0.5} \sinh\left(A\left(\frac{m^*}{m_0}\right)\frac{T}{\langle H \rangle}\right)]$ vs $1/H$ plot and dividing the slope by the factor $A\left(\frac{m^*}{m_0}\right)$ (Fig. 10). For the calculation of the extremal area of the Fermi surface, we use the Onsager relation, $F = \left(\frac{\vartheta_0}{2\pi^2}\right)S_f$; here $\vartheta_0 = 2\pi\hbar/e$ is the flux quantum, and $S_f = \pi k_f^2$ is the extremal area of the Fermi surface normal to the magnetic field. Here k_f is the Fermi wave vector. The Fermi velocity is calculated using $v_f = \frac{\hbar k_f}{m^*}$. The scattering rate (τ_s) is calculated from the Dingle temperature using the relation $\tau_s = \frac{\hbar}{2\pi k_B T_D}$, the mean free path is given by $l_D = v_f \tau_s$, and the mobility is calculated using the relation $\mu = \frac{e\tau}{m^*}$.

APPENDIX C: ELECTRONIC BAND STRUCTURE CALCULATION

We modeled the GdV₆Sn₆ material considering the hexagonal P_6/mmm space group in its ferromagnetic structure. The optimized lattice parameters $a = 5.518$ Å and $c = 9.265$ Å are close to the experimental values $a = 5.5348(7)$ and $c = 9.1797(11)$ Å [22]. The obtained magnetic moments in the V d and Gd f orbitals are $-0.147 \mu_B$ and $-6.928 \mu_B$, respectively. This indicates that the Gd f states dominate the ferromagnetic state in this material.

After optimization of the structure, we calculate the electronic band structure through band structure and projected density of states. Figure 11(a) depicts the band structure at the high-symmetry points in the irreducible Brillouin zone. The band structure depicts the well-known flat bands induced by the kagome structure (~ 0.35 eV), mainly due to the vanadium d orbitals [22]. Near the Fermi level, Dirac-like dispersion relations are observed at the K symmetry point due to the


 FIG. 10. Dingle temperature calculation for (a) frequency F_3 , (b) F_6 , (c) F_7 , and (d) F_8 .

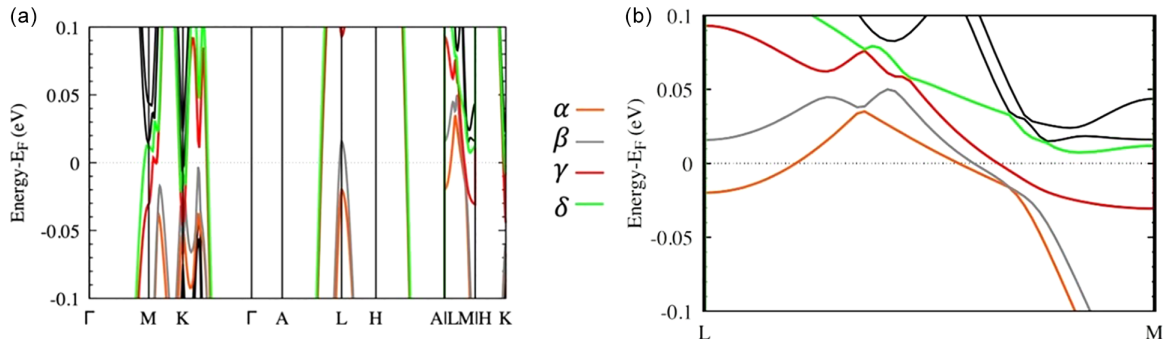
hexagonal symmetry of the kagome lattice. We also note that bands have some linear dispersion at the M point and in the Γ - K path. The band structure evidences an apparent metallic anisotropic behavior with a large band gap energy at the Γ - A path but conduction states along the L - M [Fig. 11(b)] and H - K paths.

In Fig. 8, we plot the band structure and the projected density of states to evidence the appearance of multiple Van Hove singularities (VHSs) near the Fermi level. In the density of states, VHSs appear as sharp changes like peaks, valleys, or cusplike structures, while in the band structure, they appear as local extrema such as saddle points, points with large curvature, or band edges. Both characteristics coincide in energy, as shown in Fig. 8. Previous density functional theory (DFT) calculations not including spin-orbit calculations evidenced the appearance of four VHSs which were labeled

as VHS_1 , VHS_2 , VHS_3 , and VHS_4 [21], in agreement with our findings, in which we have included the spin-orbit coupling (SOC) effect and considered the ferromagnetic phase. As expected, the SOC effect generates band splitting and a potential change in the VHS form, energy of appearance, and quantity. For example, we also observed one more VHS_5 and potentially another at -0.5 eV. All these points appear at the M high-symmetry point. Our SOC calculations evidence that the VHSs are mainly formed by the d orbitals of the vanadium kagome lattice.

APPENDIX D: FERMI SURFACE

We have obtained the Fermi surface through first-principles calculation, employing the optimized ferromagnetic structure.


 FIG. 11. (a) Band structure of ferromagnetic GdV_6Sn_6 and (b) band structure along the L - M line of the Brillouin zone, zoomed in from $+100$ to -100 meV. The four electronic bands (α , β , γ , and δ) crossing the Fermi level are depicted in distinct colors.

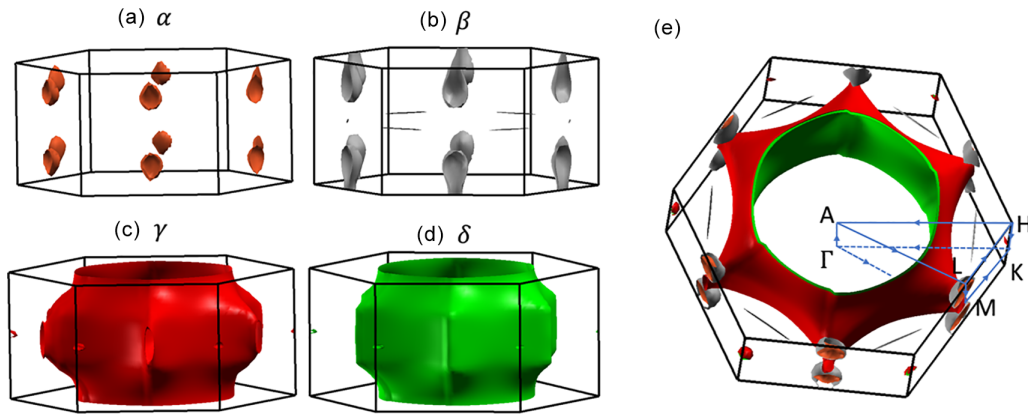


FIG. 12. Projection of the Fermi surfaces of ferromagnetic GdV_6Sn_6 at the Fermi energy: (a) band α , (b) band β , (c) band γ , (d) band δ , and (e) all Fermi surface pockets. In (e) is depicted the high-symmetry path followed to plot the band structure. All bands are depicted in different colors.

In this analysis, we have discerned four distinct electronic bands: α , β , γ , and δ . The Fermi surfaces have been projected at the Fermi energy, indicating that all observed bands intersect with this critical energy level. Notably, band α and band β exhibit holelike characteristics, while band γ and band δ predominantly demonstrate electronlike behavior. Regard-

ing the Fermi surface shapes, bands α and β exhibit irregular lobes or pockets along the M - L high-symmetry direction (see band structure of Figs. 7(a) and 10(a)]. Conversely, bands γ and δ display barrel-like shapes with prominent and open regions along the same M - L high-symmetry direction, as illustrated in Fig. 12.

-
- [1] N. J. Ghimire and I. I. Mazin, Topology and correlations on the kagome lattice, *Nat. Mater.* **19**, 137 (2020).
- [2] K. Jiang, T. Wu, J.-X. Yin, Z. Wang, M. Z. Hasan, S. D. Wilson, X. Chen, and J. Hu, Kagome superconductors AV_3Sb_5 ($A = \text{K}, \text{Rb}, \text{Cs}$), *Natl. Sci. Rev.* **10**, nwac199 (2023).
- [3] T. Neupert, M. M. Denner, J.-X. Yin, R. Thomale, and M. Z. Hasan, Charge order and superconductivity in kagome materials, *Nat. Phys.* **18**, 137 (2022).
- [4] H.-Y. Ma, J.-X. Yin, M. Zahid Hasan, and J. Liu, Magnetic and charge instabilities in vanadium-based topological kagome metals, *Phys. Rev. B* **106**, 155125 (2022).
- [5] J.-X. Yin, B. Lian, and M. Z. Hasan, Topological kagome magnets and superconductors, *Nature (London)* **612**, 647 (2022).
- [6] Y.-X. Jiang *et al.*, Unconventional chiral charge order in kagome superconductor KV_3Sb_5 , *Nat. Mater.* **20**, 1353 (2021).
- [7] J.-X. X. Yin *et al.*, Quantum-limit Chern topological magnetism in TbMn_6Sn_6 , *Nature (London)* **583**, 533 (2020).
- [8] H. Yang, Y. Sun, Y. Zhang, W. J. Shi, S. S. P. Parkin, and B. Yan, Topological Weyl semimetals in the chiral antiferromagnetic materials Mn_3Ge and Mn_3Sn , *New J. Phys.* **19**, 015008 (2017).
- [9] H. Li, B. Ding, J. Chen, Z. Li, Z. Hou, E. Liu, H. Zhang, X. Xi, G. Wu, and W. Wang, Large topological Hall effect in a geometrically frustrated kagome magnet Fe_3Sn_2 , *Appl. Phys. Lett.* **114**, 192408 (2019).
- [10] Z. Lin *et al.*, Flatbands and emergent ferromagnetic ordering in Fe_3Sn_2 kagome lattices, *Phys. Rev. Lett.* **121**, 096401 (2018).
- [11] C. Liu *et al.*, Spin excitations and spin wave gap in the ferromagnetic Weyl semimetal $\text{Co}_3\text{Sn}_2\text{S}_2$, *Sci. China Phys. Mech. Astron.* **64**, 217062 (2021).
- [12] Q. Wang, Y. Xu, R. Lou, Z. Liu, M. Li, Y. Huang, D. Shen, H. Weng, S. Wang, and H. Lei, Large intrinsic anomalous Hall effect in half-metallic ferromagnet $\text{Co}_3\text{Sn}_2\text{S}_2$ with magnetic Weyl fermions, *Nat. Commun.* **9**, 3681 (2018).
- [13] D. F. Liu *et al.*, Magnetic Weyl semimetal phase in a kagome crystal, *Science* **365**, 1282 (2019).
- [14] M. Kang *et al.*, Topological flat bands in frustrated kagome lattice CoSn , *Nat. Commun.* **11**, 4004 (2020).
- [15] W. Ma *et al.*, Rare earth engineering in RMn_6Sn_6 ($R = \text{Gd-Tm}, \text{Lu}$) topological kagome magnets, *Phys. Rev. Lett.* **126**, 246602 (2021).
- [16] X. Zhang *et al.*, Electronic and magnetic properties of intermetallic kagome magnets RV_6Sn_6 ($R = \text{Tb-Tm}$), *Phys. Rev. Mater.* **6**, 105001 (2022).
- [17] F. Kabir *et al.*, Unusual magnetic and transport properties in HoMn_6Sn_6 kagome magnet, *Phys. Rev. Mater.* **6**, 064404 (2022).
- [18] Z.-Y. Lv, Q. Jiang, J.-M. Wang, H.-J. Qian, D.-Y. Wang, S. Qiao, and M. Ye, Orbital hybridization in kagome metal GdV_6Sn_6 revealed by resonant ARPES, *Phys. Status Solidi RRL* **17**, 2300083 (2023).
- [19] H. Ishikawa, T. Yajima, M. Kawamura, H. Mitamura, and K. Kindo, GdV_6Sn_6 : A multi-carrier metal with non-magnetic $3d$ -electron kagome bands and $4f$ -electron magnetism, *J. Phys. Soc. Jpn.* **90**, 124704 (2021).
- [20] J. Lee and E. Mun, Anisotropic magnetic property of single crystals RV_6Sn_6 ($R = \text{Y}, \text{Gd-Tm}, \text{Lu}$), *Phys. Rev. Mater.* **6**, 083401 (2022).
- [21] Y. Hu, X. Wu, Y. Yang, S. Gao, N. C. Plumb, A. P. Schnyder, W. Xie, J. Ma, and M. Shi, Tunable topological dirac surface

- states and Van Hove singularities in kagome metal GdV_6Sn_6 , *Sci. Adv.* **8**, eadd2024 (2022).
- [22] G. Pokharel, S. M. L. Teicher, B. R. Ortiz, P. M. Sarte, G. Wu, S. Peng, J. He, R. Seshadri, and S. D. Wilson, Electronic properties of the topological kagome metals YV_6Sn_6 and GdV_6Sn_6 , *Phys. Rev. B* **104**, 235139 (2021).
- [23] S. Peng *et al.*, Realizing kagome band structure in two-dimensional kagome surface states of RV_6Sn_6 ($R = \text{Gd}, \text{Ho}$), *Phys. Rev. Lett.* **127**, 266401 (2021).
- [24] G. Kresse and J. Hafner, *Ab initio* molecular dynamics for liquid metals, *Phys. Rev. B* **47**, 558 (1993).
- [25] G. Kresse and D. Joubert, From ultrasoft pseudopotentials to the projector augmented-wave method, *Phys. Rev. B* **59**, 1758 (1999).
- [26] G. Kresse and J. Furthmüller, Efficiency of *ab-initio* total energy calculations for metals and semiconductors using a plane-wave basis set, *Comput. Mater. Sci.* **6**, 15 (1996).
- [27] J. P. Perdew, K. Burke, and M. Ernzerhof, Generalized gradient approximation made simple, *Phys. Rev. Lett.* **77**, 3865 (1996).
- [28] P. E. Blöchl, Projector augmented-wave method, *Phys. Rev. B* **50**, 17953 (1994).
- [29] H. J. Monkhorst and J. D. Pack, Special points for Brillouin-zone integrations, *Phys. Rev. B* **13**, 5188 (1976).
- [30] S. L. Dudarev, G. A. Botton, S. Y. Savrasov, C. J. Humphreys, and A. P. Sutton, Electron-energy-loss spectra and the structural stability of nickel oxide: An LSDA+ U study, *Phys. Rev. B* **57**, 1505 (1998).
- [31] G. Pizzi *et al.*, Wannier90 as a community code: New features and applications, *J. Phys.: Condens. Matter* **32**, 165902 (2020).
- [32] P. M. C. Rourke and S. R. Julian, Numerical extraction of de Haas–van Alphen frequencies from calculated band energies, *Comput. Phys. Commun.* **183**, 324 (2012).
- [33] I. Lifshitz and A. Kosevich, Theory of magnetic susceptibility in metals at low temperatures, *Sov. Phys. JETP* **2**, 636 (1956).
- [34] D. Shoenberg, *Magnetic Oscillations in Metals* (Cambridge University Press, Cambridge, 1984).
- [35] A. Alexandradinata and L. Glazman, Fermiology of topological metals, *Annu. Rev. Condens. Matter Phys.* **14**, 261 (2023).
- [36] C. Schindler, D. Gorbunov, S. Zherlitsyn, S. Galeski, M. Schmidt, J. Wosnitzer, and J. Gooth, Strong anisotropy of the electron-phonon interaction in NbP probed by magnetoacoustic quantum oscillations, *Phys. Rev. B* **102**, 165156 (2020).
- [37] A. Alexandradinata, C. Wang, W. Duan, and L. Glazman, Revealing the topology of Fermi-surface wave functions from magnetic quantum oscillations, *Phys. Rev. X* **8**, 011027 (2018).
- [38] A. Alexandradinata and L. Glazman, Semiclassical theory of Landau levels and magnetic breakdown in topological metals, *Phys. Rev. B* **97**, 144422 (2018).
- [39] R. Chapai *et al.*, Magnetic breakdown and topology in the kagome superconductor CsV_3Sb_5 under high magnetic field, *Phys. Rev. Lett.* **130**, 126401 (2023).
- [40] K. Shrestha *et al.*, Nontrivial Fermi surface topology of the kagome superconductor CsV_3Sb_5 probed by de Haas–van Alphen oscillations, *Phys. Rev. B* **105**, 024508 (2022).
- [41] D. Di Sante *et al.*, Flat band separation and robust spin Berry curvature in bilayer kagome metals, *Nat. Phys.* **19**, 1135 (2023).
- [42] E. Rosenberg, J. DeStefano, Y. Lee, C. Hu, Y. Shi, D. Graf, S. M. Benjamin, L. Ke, and J.-H. Chu, Quantum oscillations measurement of the heavy electron mass near the Van Hove singularity in a kagome metal, [arXiv:2401.14699](https://arxiv.org/abs/2401.14699) [Phys. Rev. B (to be published)].
- [43] R. Chapai, D. A. Browne, D. E. Graf, J. F. DiTusa, and R. Jin, Quantum oscillations with angular dependence in PdTe_2 single crystals, *J. Phys.: Condens. Matter* **33**, 035601 (2021).
- [44] J. F. DiTusa, R. G. Goodrich, N. Harrison, and E. S. Choi, Fermi surface of $\text{Cr}_{1-x}\text{V}_x$ across the quantum critical point, *Phys. Rev. B* **82**, 075114 (2010).